Efficiency evaluation of the redox reaction using Fe(II)-g-C_3N_4 for the removal of hexavalent chromium from water

Milad Fathi[a], Aziz babapoor[a*], Zohreh Rahimi-Ahar[b], Hadi Basharnavaz[c]

[a] *Department of Chemical Engineering, University of Mohaghegh Ardabili, Ardabil, Iran.*

[b] *Department of Chemical Engineering, Engineering Faculty, Velayat University, Iranshahr, Iran.*

[c] *Department of chemistry, University of Mohaghegh Ardabili, Ardabil, Iran Iran.*

Abstract

Chromium (Cr) exists in various forms in surface water and groundwater. The high solubility and mobility of Cr(VI) make it a very hazardous material that pollutes water and soil ecosystems. In this study, Fe(II)-g-C_3N_4 was synthesized using melamine and $FeCl_3.6H_2O$ via the thermal calcination method. Fe(II)-g-C_3N_4 was analyzed by XRD, FTIR, SEM, and DLS. It was shown that the g-C_3N_4 structure is a suitable distributor and stabilizer for iron particles. g-C_3N_4 reduced the accumulation of iron particles, increasing the efficiency of the redox reaction between Fe(II) and Cr(VI). The removal efficiency of Cr(VI) was influenced by pH, temperature, and the concentrations of Fe(II)-g-C_3N_4 and Cr(VI). Lower pH values, higher Fe(II)-g-C_3N_4 concentrations, and elevated temperature improved the k_{obs} and Cr(VI) elimination from water. Cr(VI) adsorption efficiency in the 30, 50, and 70 ppm solutions by Fe(II)-g-C_3N_4 nanoparticles was 99%, 93.9%, and 80.7%, respectively. Furthermore, the highest k_{obs} (0.0835 min^{-1}) was observed at a 30 ppm Cr(VI) concentration.

Keywords:

Divalent iron; Graphitic carbon nitride; Redox; Hexavalent chromium; Separation

* Corresponding author.
babapoor@uma.ac.ir, Babapoor2006@yahoo.com (A. Babapoor), Phone Number: 04531505748.

1. Introduction

Chromium (Cr) exists in trivalent and hexavalent forms (Cr(III) and Cr(VI)) depending on the pH and redox conditions [1]. Cr(III) exhibits low solubility in aqueous environments [1] and Cr(VI) represents the most harmful chromium species [2]. Cr(VI) exhibits 100 times more toxicity than Cr(III). It enhances cellular mutation probability, consequently, the cancer effect by 1000 times compared to Cr(III) [3]. Cr(VI) in water poses serious ecological and environmental risks [4]. It primarily exists as chromate (CrO_4^{2-}) and dichromate ($Cr_2O_7^{2-}$) [5]. Iron (Fe) plays a crucial role in various pollutant removal techniques, including redox, catalytic, photocatalytic, chemical precipitation, electrochemical, and adsorption. With a redox potential of about -0.44 Volts (E_0 = -0.44 V), Fe emerges as an ideal candidate for redox reactions [6]. While numerous materials have been employed for Cr(VI) removal from water, divalent and zero-valent iron (Fe(II) and Fe^0) have gained widespread acceptance in treatment applications [7]. Bioresource-based nanoparticles should be considered to avoid hazardous chemicals and processes [8, 9]. Algae-derived nitrogen-doped carbon nanoflakes fabricated with nickel ferrite is a Fe-based material for removal of Rhodamine B, Congo Red dyes [10], and antibiotics [11].

Cr(VI) equilibrium and adsorption kinetics in poly-high internal phase emulsion/single-walled carbon nanotubes (PHIPE/SW-CNT) aligned with Langmuir models and the pseudo-second-order, respectively. The highest adsorption capacity of 72.35 mg g^{-1} led to successful Cr(VI) removal [12]. The pirulina-based synthesis of mesoporous iron oxide nanoparticles led to a Cr(VI) adsorption efficiency of 92.8505 mg g^{-1} in an aqueous solution [13]. Spirulina-based TiO_2@CTAB nanoparticles were the more successful option due to higher Cr(VI) removal efficiency (127.551 mg g^{-1}) [14].

Electrospinning emerged as a highly effective technique for creating unique porous membranes to remove Cr(VI) and electrospun nanofiber membrane was identified as an effective adsorbent

[15]. Modified ceramic filters with a flux of 289 L $m^{-2}h^{-1}$ removed Cr(III) by 40% [16]. Polyvinyl alcohol-alumina film demonstrated effective elimination of Cr(VI) from wastewater at elevated concentrations [17]. The lack of selectivity of sorbent targeting CrO_4^{2-} was improved using polyethylenimine-based adsorbents [18]. Chromolaena odorata-derived magnetite nanoparticles with the highest adsorption capacity of 173.12 mg g^{-1} were introduced as promising options for Cr(VI) elimination from wastewater [19]. Nitrogen-doped coconut granulated activated carbon had the highest adsorption capacity of ~15.2 mg g^{-1}. Besides, equilibrium results best fit with Redlich-Peterson and Sips isotherm models [20]. The electrochemical process was superior to the conventional chemical processes in the remediation of Cr-contaminated groundwater [21].

When divalent iron was doped into Mg-Al layered double hydroxide, Cr(VI) effectually reduced and experimented with the Cr(III) hydroxide ($Cr(OH)_3$) redox process [22]. The adsorption process followed Langmuir-type adsorption, achieving the highest adsorption capacity of 12.5 mmol g^{-1}. Humic acids (HAs) affected the reduction of Cr(VI) to Cr(III) at a primary Cr(VI) concentration of 100 µg L^{-1}, pH of 6.5-8, and ferrous sulfate dosages of 0.25-2 mg Fe(II)/L [23]. Higher pH levels and lower Fe(II) doses resulted in elevated residual Cr concentrations. Fe(II) reduced Cr(VI) with an adsorption efficiency of approximately 100% in the pH ranging from 3 to 9, while the reduction of Cr(VI) reduced to about 60% when accounting for Fe(II) oxygenation at a pH of 12 [24]. Synthesized Fe^0-chitosan nanoparticles were examined to uptake Cr(VI) from water [7]. The reaction rate constants correlated with temperature increase and iron surface loading on the adsorbent, while inversely relating to pH and Cr(VI) concentration. The activation energy of 33 kJ mol^{-1} indicated a chemically controlled reaction mechanism. Research indicates that Fe^0 and Fe^{2+} demonstrate limited effectiveness in their pure state for removing Cr(VI) from aqueous solutions due to the accumulation of iron particles. This means that Fe^0 or Fe^{2+} should be loaded onto a unique

structure of materials (such as bentonite and chitosan), enabling a proper and homogeneous distribution of iron particles across the support structure's surface. The homogeneous distribution maximizes the effective collision between Fe and Cr(VI) in an aqueous medium, increasing the redox reaction efficiency [25].

Support materials are typically selected for their dual adsorptive and catalytic capabilities. Graphitic carbon nitride (g-C_3N_4) is inherently adsorbent and has catalytic and photocatalytic characteristics [26]. Therefore, g-C_3N_4 nanoparticles are good candidates for Fe^{2+} support and homogeneous distribution [27, 28]. Integrating the fibrous silica iron (FSFe) catalyst to g-C_3N_4 reduced the band gap. It successfully improved Cr(VI) and methyl orange (MO) degradation by 38.16% and 98.08%, respectively. The enhanced photocatalytic performance for Cr(VI) resulted from the reduced bandgap of the catalysts [29].

In this research, the elimination of Cr(VI) by the redox reaction between Fe(II) and Cr(VI) on the surface of Fe(II)-g-C_3N_4 nanoparticles was investigated. Fe(II)-g-C_3N_4 was synthesized, and the effects of pH, Fe(II)-g-C_3N_4 concentration, initial concentration of Cr(VI), and temperature on the kinetics of the Cr(VI) removal process were investigated. g-C_3N_4 would play a significant role in the Cr(VI) reduction by Fe^{2+} nanoparticles. It is expected that Fe^{2+} nanoparticles will be loaded completely uniformly on g-C_3N_4, and the synthesized nanoparticles show very high efficiency in different environmental conditions compared to previous research.

2. Materials and methods

The specifications of the chemicals used in the material synthesis and testing stages are as follows: melamine ($C_3H_6N_6$), ferric chloride hexahydrate ($FeCl_3.6H_2O$), iron(II) sulfate heptahydrate ($FeSO_4.7H_2O$), sodium thiosulfate ($Na_2S_2O_3$), sodium hydroxide (NaOH), hydrochloric acid (HCl), and potassium dichromate ($K_2Cr_2O_7$). All materials used in the experiments were from Merck company (Germany) with a purity of 98% or higher.

2.1. Pure g-C_3N_4 preparation

6.3 g of melamine was dissolved in 100 mL of deionized water at 100 °C. It was mixed with 5 mL of HCl on a magnetic stirrer for 30 min and a white precipitate was formed. After cooling the solution, it was dried at 80 °C for 24 hours. The dried precipitate was positioned in a tube furnace and heated in a semi-closed system at a temperature increase rate of 10 °C/min to an ending temperature of 550 °C for 3 hours. After cooling the content of the furnace to ambient temperature, a yellow compound (g-C_3N_4) was obtained. In the end, the synthesized g-C_3N_4 was completely pulverized in a mortar [30].

2.2. Fe(II)-g-C_3N_4 synthesis

First, 100 mL of deionized water was heated to 100 °C, then 5 mL of HCl, 6.3 g of melamine, and 1.49 g of $FeCl_3.6H_2O$ were simultaneously added to the water. The suspension was stirred using a magnet for 30 min and then stored in an oven at 80 °C for 24 hours to dry completely. The dried homogeneous mixture was placed in a semi-closed system inside the tube furnace and heated during the calcination. In this way, the mixture reached a temperature of 310 ˚C at a temperature increase rate of 10 ˚C/min. The mixture was heated at this temperature for 1 hour. Then, it was heated up to 460 ˚C and 550 ˚C at the same rate of temperature increase for 1 hour (Fig. 1). After these steps, Fe(II)-g-C_3N_4 nanoparticles were synthesized [30]. Iron has a higher density than water and is insoluble in it. It easily settled in the aqueous environment and could be separated after the completion of the reaction.

2.3. Characterization techniques and devices

The X-ray diffraction (XRD) pattern was obtained by the Panalytical device (X'pert model) with a copper source. The infrared spectroscopy was conducted using the Perkin device (RXI model). The spectra of FTIR were recorded via the Perkin Elmer device (RXI model). SEM images were taken using the Tescan (Mira3 FE-SEM model). The spectra of zeta potential and average particle size were measured by the Horiba SZ-100Z2 dynamic light scattering (DLS)

machine. Cr(VI) concentration was determined during the experiments using the Shimadzu AA-6200 atomic absorption spectrophotometer.

2.4. Batch experiments

To compare the adsorption efficiency of Cr(VI) by g-C_3N_4 and Fe(II)-g-C_3N_4, initial solutions of Cr(VI) at 30, 50, and 70 ppm were prepared. 25 mL of each prepared solution was added to either g-C_3N_4 (0.025 g) or Fe(II)-g-C_3N_4 (0.05 g). The containers were then sealed with foil and positioned in a shaker incubator operating at 250 rpm and 45 °C for designated durations. Sampling was performed to evaluate the concentration of Cr(VI) on the 22 µm membrane at different time intervals.

3. Results and discussion

3.1. Characterization

3.1.1. XRD

The XRD patterns of Fe(II)-g-C_3N_4 and g-C_3N_4 structures exhibit comparable characteristics (Fig. 2). In g-C_3N_4, the strongest peak emerged at 27.45°, representing the accumulation of layers of aromatics that are indexed for graphitic material as a (002) plane. The (002) plane shows an interlayer distance of 325 nm. Additionally, in the g-C_3N_4 XRD pattern, the peak at ~13.1° corresponds to the (100) plane and shows the structural packing in-plane. When Fe(II) is incorporated into the g-C_3N_4 structure, it diminishes the intensity of g-C_3N_4 peaks. Fe ions disrupt the thermal condensation process of melamine and cause the growth of g-C_3N_4 crystallization, thereby reducing g-C_3N_4 crystallinity. In addition, the XRD spectrum of Fe(II)-g-C_3N_4 nanoparticles shows no peaks attributed to Fe(II) phases. It is attributed to the proper and homogeneous dispersion of Fe(II) in the structure of g-C_3N_4.

3.1.2. FTIR

Fig. 3 shows the FTIR spectra comparing Fe(II)-g-C_3N_4 and g-C_3N_4. The FTIR spectra of g-C_3N_4 exhibits distinct peaks within 1165-1200 cm^{-1}, indicating the tensile forms of C-N heterocycles. Furthermore, the peak corresponding to its triazine units is shown at 807.43 cm^{-1}. The peaks in the range of 2900-3500 cm^{-1} indicate the vibrational and tensile states of N-H. This peak shows the amino acids' presence, even after direct heat treatment on the melamine. The FTIR spectrum of Fe(II)-g-C_3N_4 shows distinct peaks at 2850-3450, 1200-1750, and 806 cm^{-1}. The peak at 806 cm^{-1} indicates the triazine units corresponding to the g-C_3N_4 structure. Peaks in 2850-3450 cm^{-1} can be attributed to N-H tensile vibrations. Moreover, the peaks observed in 1200-1750 cm^{-1} are related to the tensile vibrations between the C-N and C=N joints. The peaks at 1205-1235 cm^{-1} become slightly more prominent due to the existence of Fe(II) in the structure and C-NH-C tensile vibration between heptazine units. Moreover, the peak at 2171 cm^{-1} shows defective C-N bonds owing to the widespread presence of Fe(II) in the g-C_3N_4 structure. These observations show that Fe(II) greatly prevents melamine condensing and crystallizing, hence, the formation of nanoparticles with increased imperfect bonds and reduced polymerization degree.

3.1.3. SEM

Figs. 4a, 4b, and 4c show the complete formation of graphitic plates and the crystallinity of g-C_3N_4 during thermal polymerization. Pure g-C_3N_4 has a typical layered structure with a cavity of 100-150 nm. Figs. 4d, 4e, and 4f show the SEM images related to Fe(II)-g-C_3N_4 nanoparticles and Fe(II) incorporation within the g-C_3N_4 framework. The size of the plates decrease, and irregular wrinkles increase owing to g-C_3N_4's partial crystallization when Fe(II) is present. Fe(II)-g-C_3N_4 demonstrates a layered structure and contains highly porous sheets.

3.1.4. DLS

Fe(II)-g-C_3N_4 was synthesized according to the instructions presented by [30]. To ensure the correct synthesis of Fe(II)-g-C_3N_4, XRD and FTIR analyses were conducted. In this study, instead of repeating all the analyses conducted by [30], DLS analysis was applied for innovation. The purpose of using DLS analysis was the evaluation of the changes in size, zeta potential, and surface charge created by adding Fe(II) to the g-C_3N_4 structure to understand whether a suitable substrate for the redox reaction is created or not. According to DLS analysis, the reduction in more negative surface charge in Fe(II)- g-C_3N_4 compared to g-C_3N_4 can be attributed to the uniform distribution and loading of Fe(II) magnetic particles in the structure and pores on the surface of the g-C_3N_4 nanoparticle, indicating that the iron nanoparticle provides a suitable environment for the redox reaction.

3.1.4.1. Average particle size

DLS measures the average size of nanoparticles. The average particle size of Fe(II)-g-C_3N_4 and g-C_3N_4 structures shows their classification as nanoparticles, with an average dimension of 550.1 nm and 486.8 nm, respectively (Figs. 5a and 5b).

3.1.4.2. Zeta potential

The surface load of g-C3N4 and Fe(II)-g-C3N4 is equal to -55.2 mV and -2 mV, respectively (Fig. 6). The reduction of the negative surface charge in Fe(II)-g-C_3N_4 relative to g-C_3N_4 can be related to the loading and uniform distribution of Fe(II) magnetic particles within the structure of g-C_3N_4 nanoparticles.

3.2. Cr(VI) removal by Fe(II)-g-C_3N_4 and g-C_3N_4

Fig. 7 presents the amount of Cr(VI) removal when using g-C3N4 and Fe(II)-g-C3N4. After one hour, Fe(II)-g-C_3N_4 demonstrates a significantly higher Cr(VI) removal efficiency (77.8%) than g-C_3N_4. In the structure of Fe(II)-g-C_3N_4, g-C_3N_4 acts as a support material and can stabilize and disperse Fe(II), thereby increasing the reactivity of Fe(II). Literature has also

confirmed that pure iron shows poor performance in Cr(VI) elimination owing to iron particles' aggregation tendency, hence, the reduction in the specific surface area and reactivity of iron [31, 32].

3.3. Kinetics studies

The reduction of Cr(VI) typically relies on how Fe(II) is distributed across the g-C_3N_4 surface. The equation of the redox reaction rate (v) between Cr and the different capacities of Fe follows a pseudo-first-order reaction normalized to the surface area as shown below [33].

$$v = -\frac{dC}{dt} = k_{SA} a_s \rho_m C \quad (1)$$

where, C presents the change in concentration of the contaminant in solution (mg L^{-1}), a_s is the specific surface area (m^2 g^{-1}), k_{SA} denotes the reaction rate under certain conditions (L $h^{-1}m^{-2}$) when introducing Fe(II) into the g-C_3N_4, and ρ_m stands for mass concentration (g L^{-1}). k_{SA}, a_s, and ρ_m can be replaced by a general rate constant called k_{obs} (Eq. 2) [33]. k_{obs} is the observed rate constant of a quasi-first-order reaction (min^{-1}) and is determined by graphing -ln(C/C_0) vs. time (min).

$$v = \ln\frac{C}{C_0} = -k_{obs} t \quad (2)$$

3.3.1. Influence of pH on Cr(VI) removal efficiency using Fe(II)-g-C_3N_4

Cr(VI) removal using Fe(II)-g-C_3N_4 was performed at the pH values of 4, 5, 7, and 8. An initial Cr(VI) concentration of 50 ppm, a temperature of 35 °C and a Fe(II)-g-C_3N_4 concentration of 1.5 g L^{-1} was considered. Based on the maximum Cr(VI) removal efficiency, it was observed that as the pH increases, the amount of k_{obs} and the removal capacity of Cr(VI) decreases (Table 1). This means that the removal efficiency of Cr(VI) is higher in acidic environments. It should be noted that the point of zero charge (PZC) of Fe(II)-g-C_3N_4 is 3.9.

3.3.2. Effect of Fe(II)-g-C_3N_4 concentration on the kinetics of Cr(VI) elimination

During the final stage of Cr(VI) removal testing, atomic absorption spectrometry is used to determine the quantity of dissolved iron. Analysis reveals zero soluble iron presence, with all Fe(II) particles integrated into g-C_3N_4. Similarly, at the end of the reaction, the concentrations of Cr(VI) and Cr(III) decrease sharply. This information shows that the oxidation of Fe(II) to Fe(III) and the reduction of Cr(VI) to Cr(III) occurs in the synergistic and redox reaction [34]. This redox reaction can be written as follows:

$$Cr_2O_7^{2-} + 6Fe^{2+} + 7H_2O = 2Cr(OH)_3^{-} + 6Fe^{3+} + 8HO^{-} \quad (3)$$

The direct use of Fe(II) in the reaction has some advantages over Fe^0. In the Cr precipitation reaction, only the divalent form of Fe is able to participate in the reaction, so Fe^0 must first be oxidized to Fe(II) in an aqueous medium and Fe^{2+} reacts with $Cr_2O_7^{2-}$. The oxidation of Fe^0 in water is accompanied by the release of OH^-, and as a result, the aqueous medium is driven to increase the pH. This increase in pH is an undesirable factor for the reaction. Therefore, the use of Fe^{2+} instead of Fe^0 can play a role in reducing the activation energy of the reaction and increasing the efficiency of the reaction. In equations 4 and 5, the two-step nature of the $Cr_2O_7^{2-}$ degradation reaction by Fe^0 can be seen [35].

$$Fe^0 + 2H_2O \rightarrow Fe^{2+} + H_2 + 2HO^{-} \quad (4)$$

$$6Fe^{2+} + Cr_2O_7^{2-} + 7H_2O \rightarrow 6Fe^{3+} + 2Cr(OH)_3^{-} + 8HO^{-} \quad (5)$$

A small percentage of Cr(VI) removal can be due to the g-C_3N_4 adsorption process, which acts as a synergistic process. This adsorption process usually occurs at non-reactive (iron-free) sites. Table 2 illustrates that the reaction rate and the percentage of Cr(VI) removal increase by an increase in the Fe(II)-g-C_3N_4 concentration. It should be noted that a temperature of 35 °C, a pH of 5, and a Cr(VI) concentration of 50 ppm were considered.

3.3.3. Influence of temperature on the kinetics of Cr(VI) removal by Fe(II)-g-C_3N_4

When temperature rises, it enhances the vibration of Cr(VI), thereby increasing the effective collision between the Fe(II)-g-C_3N_4 surface and Cr(VI) [36]. The water-soluble oxygen is also reduced, reducing the effectiveness of oxygen as a competitor for Cr(VI) in entering the redox reaction with Fe(II) (Eq. 6) [20]. All these phenomena lead to an increase in the k_{obs} by increasing the solution temperature (Fig. 8).

$$2Fe^{2+} + {}^{1}/_{2}O_2 + H_2O = 3Fe^{3+} + 2HO^{-} \quad (6)$$

Table 3 tabulates supplementary data concerning the impact of temperature changes on the Cr(VI) removal efficiency.

By calculating the slope of the graph showing ln(k_{obs}) against temperature (*1/T*), and applying the Arrhenius formula (Eq. 7), the apparent activation energy (E_a) is derived (Fig. 9) [25,37]:

$$\ln k_{obs} = -\frac{E_a}{RT} + \ln A_0 \quad (7)$$

Eq. (7) yields an E_a of 26.9 kJ mol^{-1}. This value can be the result of both the redox and the adsorption processes. Notably, E_a values exceeding 21 kJ mol^{-1} indicate chemical reactions. The reaction of reducing Cr(VI) by iron is surface-mediated. It involves the following steps: adsorption of Cr(VI) on the surface of iron; the transfer of Cr(VI) (containing molecules) to the iron surface; electron exchange from Fe(II) to Cr(VI) and Cr(III) as the final product.

3.3.4. Influence of Cr(VI) concentration on the kinetics of Cr(VI) removal

The Cr(VI) removal efficiency and the reaction rate constant highly depend on the Cr(VI) concentration. Higher Cr(VI) concentrations lead to decreased rate constants and Cr(VI) removal percentage (Table 4). Cr(VI) is a strong oxidizer for iron particles, and by increasing Cr(VI) concentration, iron particles become more oxidized and lose their Cr(VI) removal property. Also, increased Cr(VI) concentrations cause faster blockage of both reactive and non-reactive sites in Fe(II)-g-C_3N_4, reducing its effectiveness [9]. Notably, reactive sites are specifically where Fe(II) is located. The mechanism of Cr(VI) elimination differs between

reactive and non-reactive sites. Reactive sites utilize redox processes for Cr(VI) elimination, while non-reactive sites employ adsorption to remove the contaminant [7].

Fe(II)-g-C_3N_4 has a high potential to be used in advanced oxidation processes. For example, nanomaterials containing positive iron ions have shown their high efficiency in activating peroxymonosulfate (PMS) for the destruction of organic pollutants with complex structures such as dyes [38]. Therefore, Fe(II)-g-C_3N_4 is a suitable candidate for use in advanced oxidation processes in future research. Application of the proper instrument (e.g., fixed bed column) are recommended to remove Cr(VI) from aqueous solutions [39].

4. Conclusion

In this research, Fe(II)-g-C_3N_4 nanoparticles were successfully synthesized. It was shown that the g-C_3N_4 structure is a suitable distributor and stabilizer for iron particles. g-C_3N_4 reduced the accumulation of iron particles, increasing the efficiency of the redox reaction between Fe(II) and Cr(VI). In addition, g-C_3N_4 removed part of the Cr(VI) from the aqueous medium by synergistic adsorption. Based on the results, the Cr (VI) removal efficiency at initial concentrations of 30, 50, and 70 ppm by Fe(II)-g-C_3N_4 nanoparticles was 99, 93.9, and 80.7%, respectively. The maximum k_{obs} (0.0835 min^{-1}) was obtained at an initial Cr(VI) concentration of 30 ppm. Furthermore, it was found that increasing the solution temperature, acidifying the environment, and increasing the concentration of Fe(II)-g-C_3N_4 strengthen the reaction to progress and thus increases the efficiency of Cr(VI) removal from wastewater. Increasing the concentration of Cr(VI) reduced the k_{obs} and Cr(VI) removal efficiency.

Declaration of Funding

This research did not receive any specific funding.

Conflict of Interest

There is no actual or potential conflict of interest concerning this article.

Data Availability Statement

The data that supports this paper is available in the article.

Nan, G., Zang, C., Dou, R., et al. \Pricing and resource allocation for multimedia social network in cloud environments", Knowledge-Based Syst., 88, pp. 1{11 (2015). https://doi.org/10.1016/j.knosys.2015.08.017.

References

[1] Oliveira, H., "Chromium as an environmental pollutant: insights on induced plant toxicity", *J. Bot.* pp. 375843 (2012). https://doi.org/10.1155/2012/375843.

[2] Liu, S., Zhang, L., Kim, H., et al. "Recent advances and challenges in monitoring Chromium ions using fluorescent probes", *Coord. Chem. Rev.*, **501** pp. 215575 (2024). https://doi.org/10.1016/j.ccr.2023.215575.

[3] Costa, M. "Potential hazards of hexavalent Chromate in our drinking water", *Toxicol. Appl. Pharmacol.*, **188** pp. 1-5 (2003). https://doi.org/10.1016/S0041-008X(03)00011-5.

[4] Juturu, R., Selvaraj, R. and Murty, V.R. "Efficient removal of hexavalent chromium from wastewater using a novel magnetic biochar composite adsorbent", *J. Water Process Eng.*, **66** pp. 105908 (2024). https://doi.org/10.1016/j.jwpe.2024.105908.

[5] Sabonian, M. and Mahanpoor, K. "Preparation of ZnO nanocatalyst supported on todorokite and photocatalytic efficiency in the reduction of Chromium (VI) pollutant from aqueous solution", *Iran. J. Catal.*, **9** pp. 201-211 (2019). https://oicepress.com/ijc/article/view/4047.

[6] Xue, X. Y., Cheng, R., Shi, L., et al. "Nanomaterials for water pollution monitoring and remediation", *Environ. Chem. Lett.*, **15** pp. 23-27 (2017). https://doi.org/10.1007/s10311-016-0595-x.

[7] Geng, B., Jin, Z., Li, T., et al. "Kinetics of hexavalent Chromium removal from water by Chitosan-Fe^0 nanoparticles", *Chemosphere*, **75** pp. 825-830 (2009). https://doi.org/10.1016/j.chemosphere.2009.01.009.

[8] Mazumder, D., Mittal, R. and Nath, S.K. "Green synthesis of silver nanoparticles from waste Vigna mungo plant and evaluation of its antioxidant and antibacterial activity", *Biomass Convers. Bioref.*, pp. 1-12 (2024). https://doi.org/10.1007/s13399-024-05375-x.

[9] Selvaraj, R., Iyer, R.V., Murugesan, G., et al. "Modeling 2, 4-dichlorophenoxyacetic acid adsorption on candle bush pod-derived activated carbon: Insights from advanced statistical physics models", *J. Water Process Eng.*, **66** pp. 106027 (2024). https://doi.org/10.1016/j.jwpe.2024.106027.

[10] Patar, S., Mittal, R., Dutta, A., et al. "Algae derived N-doped mesoporous carbon nanoflakes fabricated with nickel ferrite for photocatalytic removal of Congo Red and Rhodamine B dyes", *Surf. Interf.*, **51** pp. 104710 (2024). https://doi.org/10.1016/j.surfin.2024.104710.

[11] Patar, S., Mittal, R., Yasmin, F., et al. "Photocatalytic degradation of antibiotics by N-doped carbon nanoflakes-nickel ferrite composite derived from algal biomass", *Chemosphere*, **363** pp. 142908 (2024). https://doi.org/10.1016/j.chemosphere.2024.142908.

[12] Binish, C.J., Vijayasankar, A.V., and Aan, M.S. "Synthesis and characterization of Poly-Vinyl Alcohol-Alumina composite film: an efficient adsorbent for the removal of Chromium (VI) from water", *Mater. Today Proceed.*, **62** pp. 5182-5188 (2022). https://doi.org/10.1016/j.matpr.2022.02.629.

[13] Mittal, R., Sharma, A., Bhardwaj, A.K., et al. "Removal of chromium (VI) using spirulina assisted synthesized mesoporous iron oxide nanoparticles". *Inorganic Chem. Commun.*, **154** pp. 110881 (2023). https://doi.org/10.1016/j.inoche.2023.110881.

[14] Mittal, R., Patar, S., Sharma, A., et al. "Surface modified novel synthesis of Spirulina assisted mesoporous TiO_2@CTAB nanocomposite employed for efficient removal of chromium (VI) in wastewater", *Appl. Surf. Sci.*, **679** pp. 161309 (2025). https://doi.org/10.1016/j.apsusc.2024.161309.

[15] Mahpishanian, S., Ahmadian-Alam, L., and Foudazi, R. "Porous polymer nanocomposites containing single-walled Carbon nanotubes for Chromium (VI) removal from water", *React. Funct. Polym.*, **192** pp. 105719 (2023). https://doi.org/10.1016/j.reactfunctpolym.2023.105719.

[16] Mohamed, A.M., Thalji, M.R., Yasin, S.A., et al. "Recent advances in electrospun fibrous membranes for effective Chromium (VI) removal from water", *J. Mol. Liq.*, **383** pp. 122110 (2023). https://doi.org/10.1016/j.molliq.2023.122110.

[17] Mahlangu, O.T., Mubiayi, M.P., and Mamba, B.B. "A facile approach for the synthesis of ceramic filters for methyl orange, Chromium and Lead removal from water", *Phys. Chem. Earth, Parts A/B/C*, **129** pp. 103368 (2023). https://doi.org/10.1016/j.pce.2023.103368.

[18] Verma, R., Maji, P.K., and Sarkar, S. "Removal of hexavalent Chromium from impaired water: Polyethylenimine-based sorbents-A review", *J. Environ. Chem. Eng.*, **11** pp. 109598 (2023). https://doi.org/10.1016/j.jece.2023.109598.

[19] Garvasis, J., Prasad, A.R., Shamsheera, K. O., et al. "A facile one-pot synthesis of phyto-conjugate superparamagnetic magnetite nanoparticles for the rapid removal of hexavalent Chromium from water bodies", *Mater. Res. Bullet.*, **160** pp. 112130 (2023). https://doi.org/10.1016/j.materresbull.2022.112130.

[20] Abushawish, A., Almanassra, I.W., Backer, S.N., et al. "High-efficiency removal of hexavalent Chromium from contaminated water using Nitrogen-doped activated carbon: Kinetics and isotherm study", *Mater. Chem. Phys.*, **291** pp. 126758 (2022). https://doi.org/10.1016/j.matchemphys.2022.126758.

[21] Mukhopadhyay, B., Sundquist, J., and Schmitz, R. J. "Removal of Cr (VI) from Cr-contaminated groundwater through electrochemical addition of Fe (II)", *J. Environ. Manag.*, **82** pp. 66-76 (2007). https://doi.org/10.1016/j.jenvman.2005.12.005.

[22] Kameda, T., Kondo, E., and Yoshioka, T. "Preparation of Mg-Al layered double hydroxide doped with Fe2+ and its application to Cr (VI) removal", *Sep. Purif. Technol.*, **122** pp. 12-16 (2014). https://doi.org/10.1016/j.seppur.2013.10.033.

[23] Gröhlich, A., Langer, M., Mitrakas, M., et al. "Effect of organic matter on Cr (VI) removal from groundwaters by Fe (II) reductive precipitation for groundwater treatment", *Water*, **9** pp. 389 (2017). https://doi.org/10.3390/w9060389.

[24] Mitrakas, M. G., Pantazatou, A. S., Tzimou-Tsitouridou, R., et al. "Influence of pH and temperature on Cr (VI) removal from a natural water using Fe (II): A pilot and full scale case study", *Desal. Water Treat.*, **33** pp. 77-85 (2011). https://doi.org/10.5004/dwt.2011.2620.

[25] Shi, L. N., Lin, Y. M., Zhang, X., et al. "Synthesis, Characterization and kinetics of Bentonite supported NZVI for the removal of Cr (VI) from aqueous solution", *Chem. Eng. J.*, **171** pp. 612-617 (2011). https://doi.org/10.1016/j.cej.2011.04.038.

[26] Nguyen, T. B., Sherpa, K., Chen, C. W., et al. "Enhancing photocatalytic reduction of Cr (VI) in water through morphological manipulation of g-C_3N_4 photocatalysts: A comparative study of 1D, 2D, and 3D structures", *Chemosphere*, **362** pp. 142787 (2024). https://doi.org/10.1016/j.chemosphere.2024.142787.

[27] Oh, W. D., Ng, C. Z., Ng, S. L., et al. "Rapid degradation of Organics by peroxymonosulfate activated with ferric ions embedded in graphitic carbon nitride", *Sep. Purif. Technol.*, **230** pp. 115852 (2020). https://doi.org/10.1016/j.seppur.2019.115852.

[28] Wen, J., Xie, J., Chen, X., et al. "A review on g-C_3N_4-based photocatalysts". *Appl. Surf. Sci.*, **391** pp. 72-123 (2017). https://doi.org/10.1016/j.apsusc.2016.07.030.

[29] Hazril, N.I.H., Abdullah, T.A.T., Abd Aziz, F.F., et al. "Simultaneous photo-removal of hexavalent chromium and methyl orange by fabrication of graphitic carbon nitride loaded on fibrous silica iron". *E3S Web of Conferences* **516** pp. 03002 (2024).

[30] Bicalho, H. A., Lopez, J. L., Binatti, I., et al. "Facile synthesis of highly dispersed Fe (II)-doped g-C_3N_4 and its application in Fenton-like catalysis", *Mol. Catal.*, **435** pp. 156-165 (2017). https://doi.org/10.1016/j.mcat.2017.04.003.

[31] Ponder, S. M., Darab, J. G., and Mallouk, T. E. "Remediation of Cr (VI) and Pb (II) aqueous solutions using supported, nanoscale zero-valent Iron", *Environ. Sci. Technol.*, **34** pp. 2564-2569 (2000). https://doi.org/10.1021/es9911420.

[32] Chen, S.S., Hsu, B.C., and Hung, L.W. "Chromate reduction by waste Iron from electroplating wastewater using plug flow reactor", *J. Hazard. Mater.*, **152** pp. 1092-1097 (2008). https://doi.org/10.1016/j.jhazmat.2007.07.086.

[33] Rivero-Huguet, M. and Marshall, W.D. "Reduction of hexavalent Chromium mediated by micron-and nano-scale zero-valent metallic particles", *J. Environ. Monit.*, **11** pp. 1072-1079 (2009). https://doi.org/10.1039/B819279K.

[34] Wang, Z., Ma, W., Chen, C., et al. "Photochemical coupling reactions between Fe (III)/Fe (II), Cr (VI)/Cr (III), and Polycarboxylates: inhibitory effect of Cr species", *Environ. Sci. Technol.*, **42** pp. 7260-7266 (2008). https://doi.org/10.1021/es801379j.

[35] Shi, L.N., Lin, Y.M., Zhang, X., et al. "Synthesis, characterization and kinetics of bentonite supported nZVI for the removal of Cr (VI) from aqueous solution", *Chem. Eng. J.*, **171** pp. 612-617 (2011). https://doi.org/10.1016/j.cej.2011.04.038.

[36] Baral, S.S., Das, N., Chaudhury, G. R., et al. "A preliminary study on the adsorptive removal of Cr (VI) using seaweed, Hydrilla Verticillata", *J. Hazard. Mater.*, **171** pp. 358-369 (2009). https://doi.org/10.1016/j.jhazmat.2009.06.011.

[37] Wang, H., Wang, S., Wang, S., et al. "Efficient metal-organic framework adsorbents for removal of harmful heavy metal Pb (II) from solution: Activation energy and interaction mechanism", *J. Environ. Chem. Eng.*, **11** pp. 109335 (2023). https://doi.org/10.1016/j.jece.2023.109335.

[38] Song, W., Xinyu X., Guanlong W., et al. "Highly efficient peroxymonosulfate activation on Fe-NC catalyst via the collaboration of low-coordinated Fe-N structure and Fe nanoparticles for enhanced organic pollutant degradation", J. *Hazard. Mater.*, **455** pp.131596 (2023). https://doi.org/10.1016/j.jhazmat.2023.131596.

[39] Samanth, A., Vinayagam, R., Varadavenkatesan, T., et al. "Fixed bed column adsorption systems to remove 2, 4-dichlorophenoxyacetic acid herbicide from aqueous solutions using magnetic activated carbon", *Environ. Res.*, **261** pp. 119696 (2024). https://doi.org/10.1016/j.envres.2024.119696.

Figure captions

Fig. 1. Steps of synthesis of Fe(II)-g-C_3N_4 by thermal calcination method

Fig. 2. XRD patterns of Fe(II)-g-C_3N_4 and g-C_3N_4

Fig. 3. FTIR patterns of Fe(II)-g-C_3N_4 and g-C_3N_4

Fig. 4. SEM images of (a, b, and c) pure g-C_3N_4 and (d, e, and f) Fe(II)-g-C_3N_4

Fig. 5. Average particle size of (a) g-C_3N_4 and (b) Fe(II)-g-C_3N_4

Fig. 6. Surface load of (a) g-C_3N_4 and (b) Fe(II)-g-C_3N_4

Fig. 7. Cr(VI) removal using Fe(II)-g-C_3N_4 and g-C_3N_4

Fig. 8. Effects of temperature on the kinetics of Cr(VI) removal by Fe(II)-g-C_3N_4 (pH: 5; Cr(VI) concentration: 50 ppm in deionized water; Fe(II)-g-C_3N_4 concentration: 2 $g.L^{-1}$; mixing with a shaking incubator at 250 rpm)

Fig. 9. Relationship between k_{obs} and temperature to obtain E_a

Table captions

Table 1. The influence of pH values on the Cr(VI) removal using Fe(II)-g-C_3N_4

Table 2. The influence of Fe(II)-g-C_3N_4 concentration on the kinetics of Cr(VI) removal

Table 3. The impact of temperature on the kinetics of Cr(VI) removal

Table 4. The impact of Cr(VI) concentration on the kinetics of Cr(VI) removal

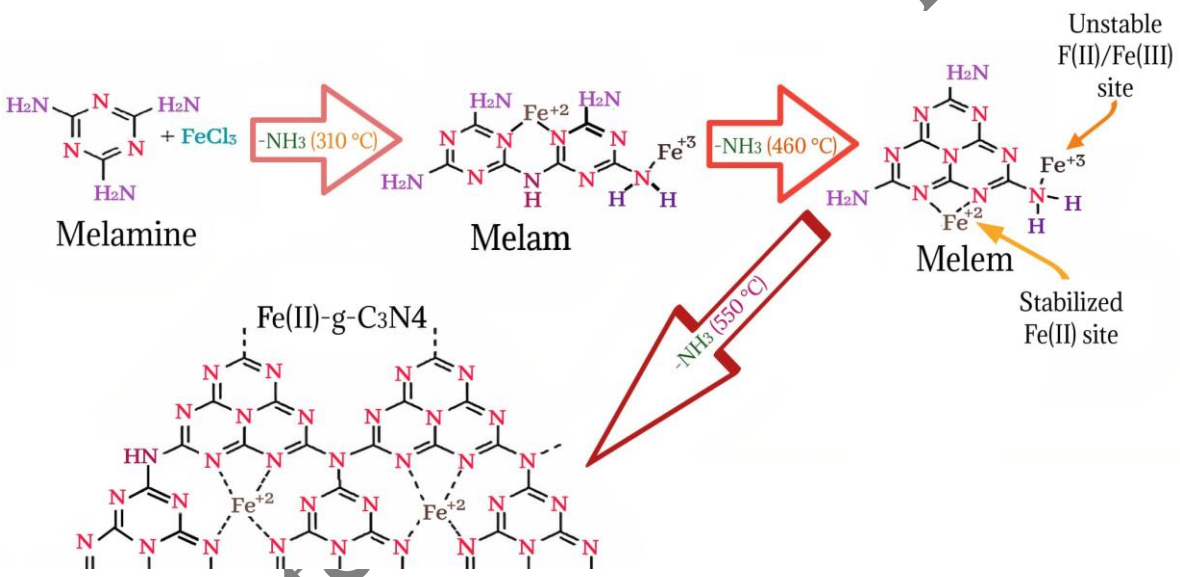

Fig. 1. Steps of synthesis of Fe(II)-g-C_3N_4 by thermal calcination method

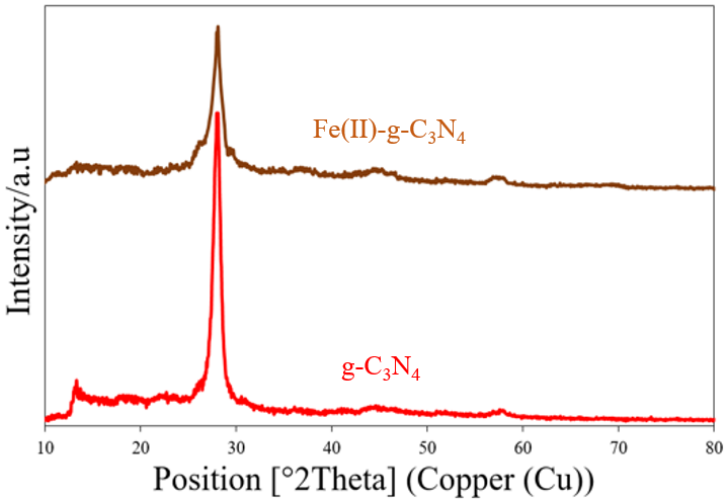

Fig. 2. XRD patterns of Fe(II)-g-C_3N_4 and g-C_3N_4

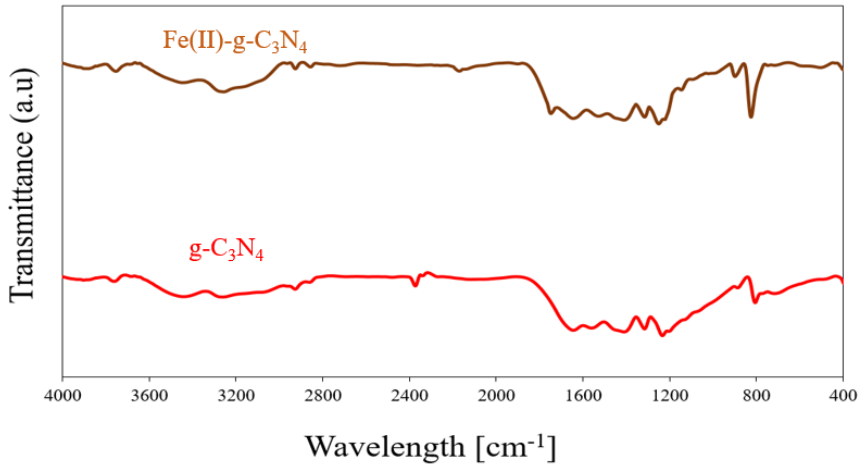

Fig. 3. FTIR patterns of Fe(II)-g-C_3N_4 and g-C_3N_4

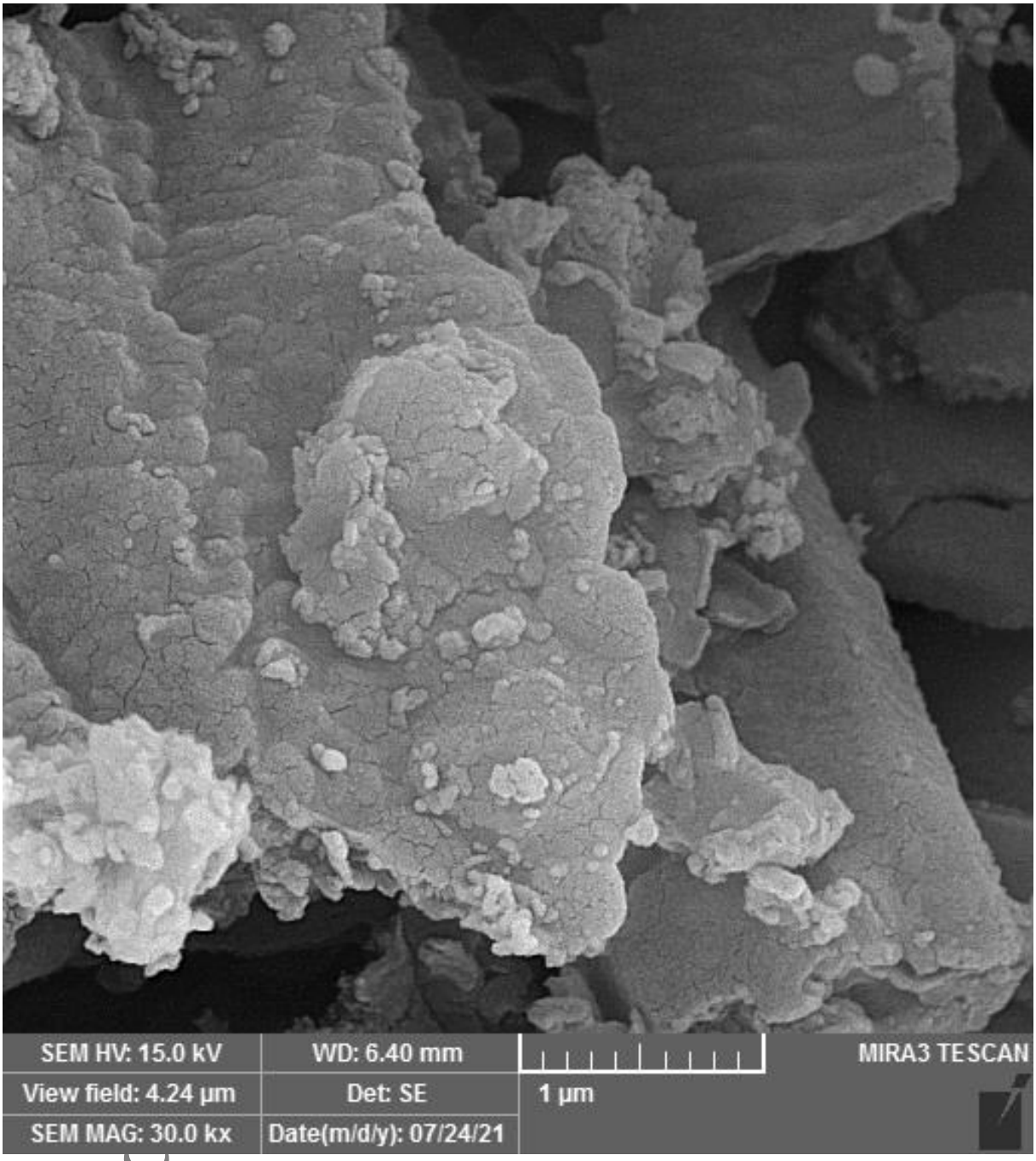
SEM HV: 15.0 kV
WD: 6.40 mm
MIRA3 TESCAN
View field: 4.24 µm
Det: SE
1 µm
SEM MAG: 30.0 kx
Date(m/d/y): 07/24/21

(a)

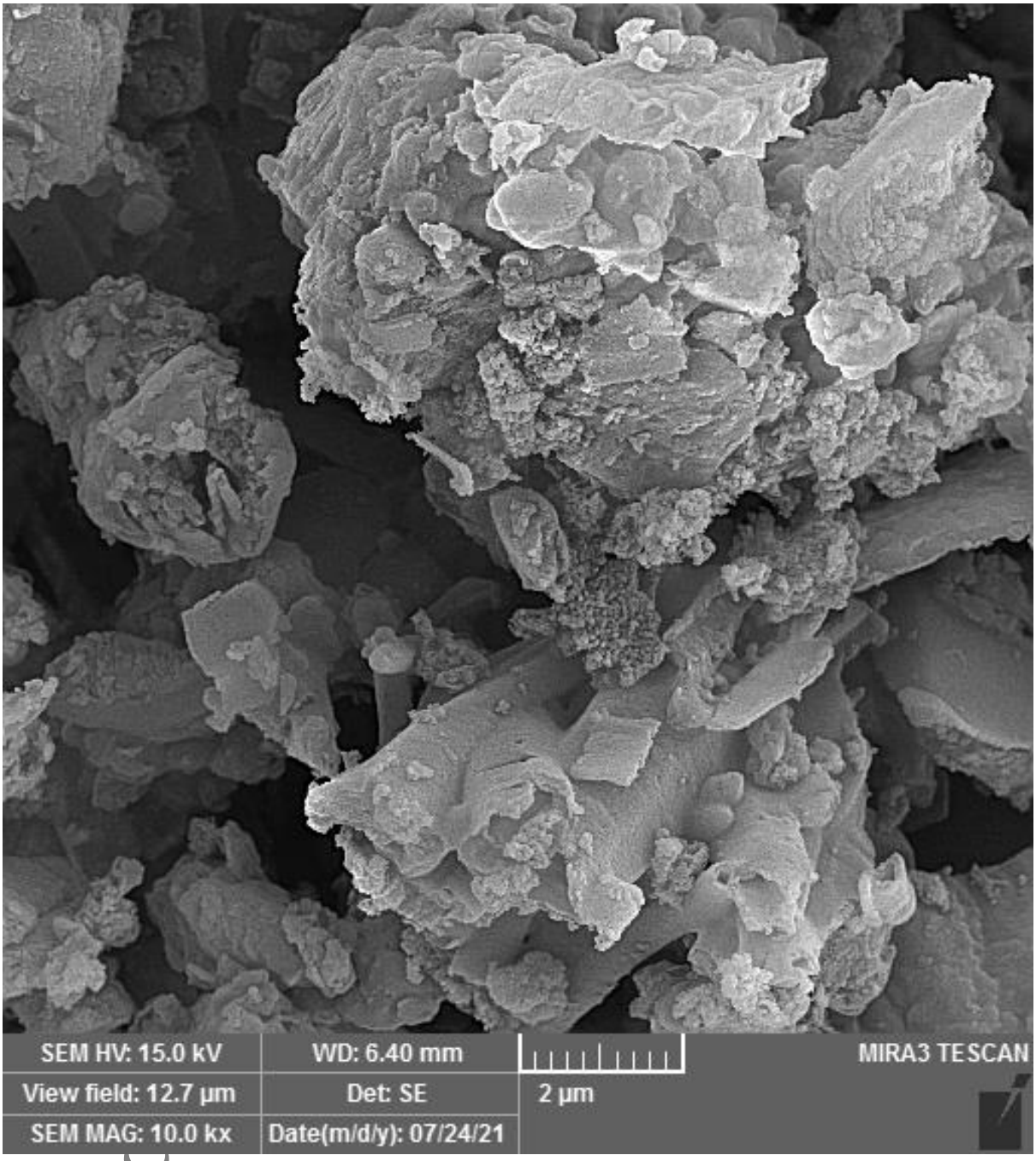
SEM HV: 15.0 kV
WD: 6.40 mm
MIRA3 TESCAN
View field: 12.7 µm
Det: SE
2 µm
SEM MAG: 10.0 kx
Date(m/d/y): 07/24/21

(b)

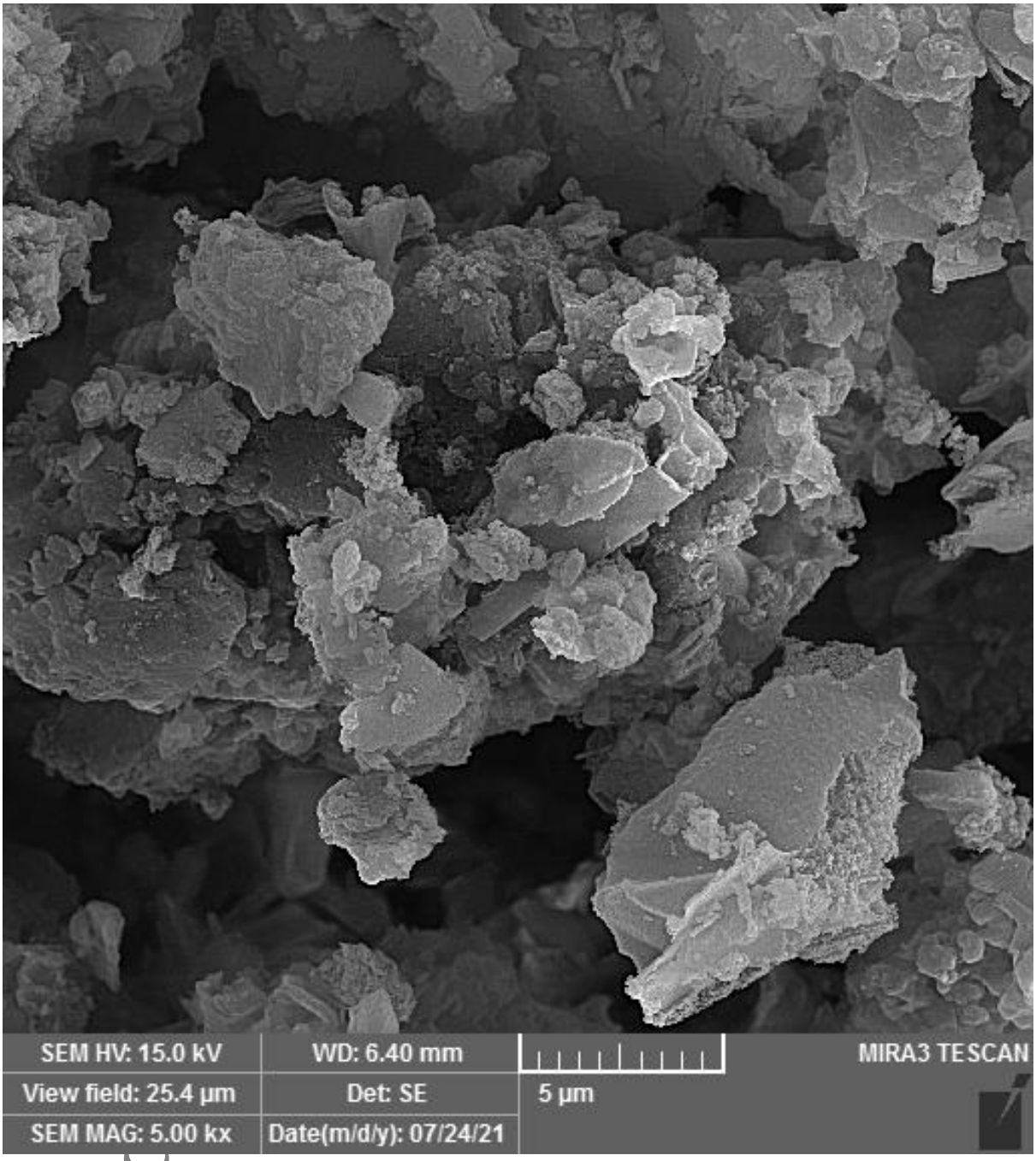
SEM HV: 15.0 kV
WD: 6.40 mm
MIRA3 TESCAN
View field: 25.4 µm
Det: SE
5 µm
SEM MAG: 5.00 kx
Date(m/d/y): 07/24/21

(c)

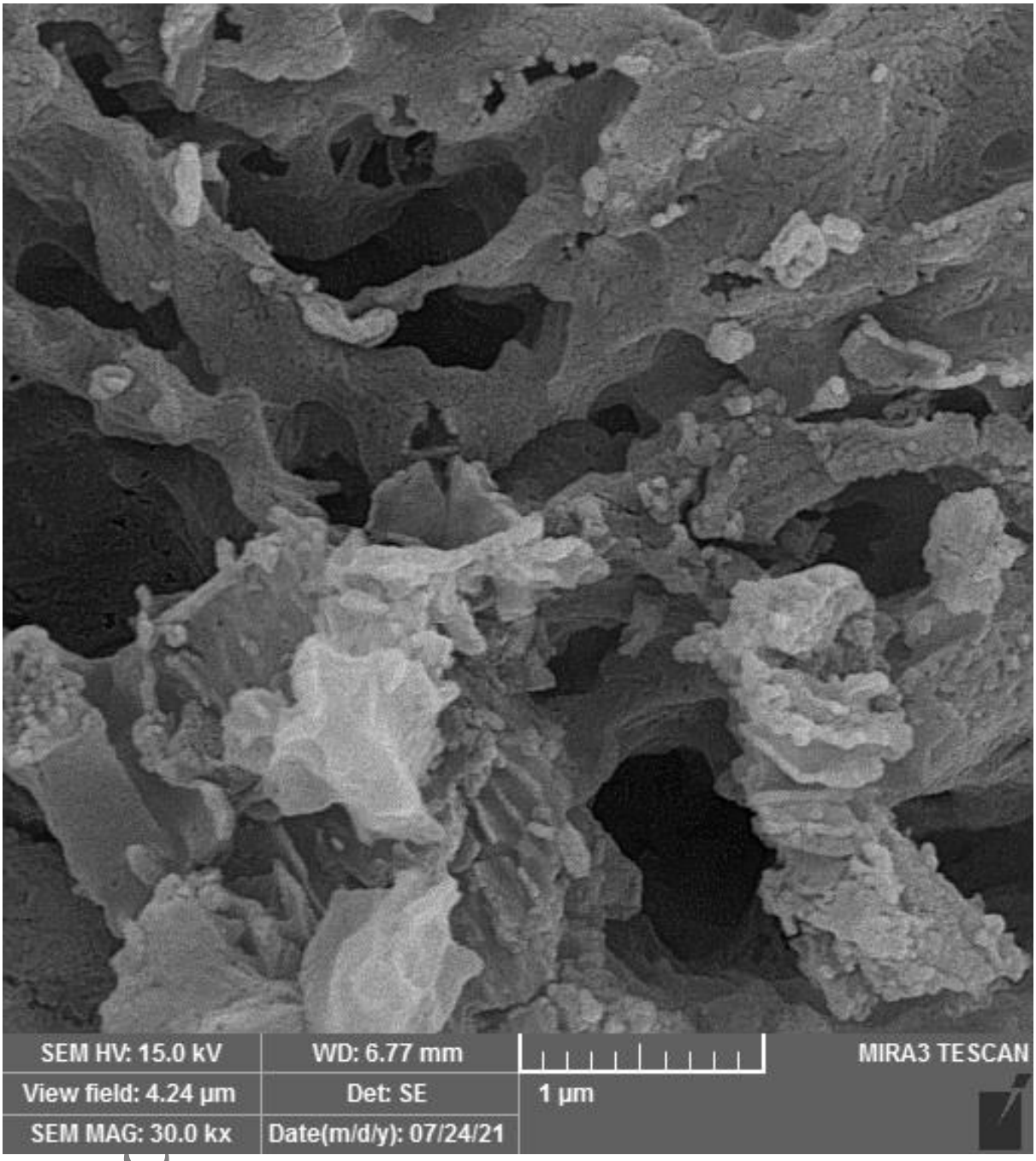
SEM HV: 15.0 kV
WD: 6.77 mm
MIRA3 TESCAN
View field: 4.24 µm
Det: SE
1 µm
SEM MAG: 30.0 kx
Date(m/d/y): 07/24/21

(d)

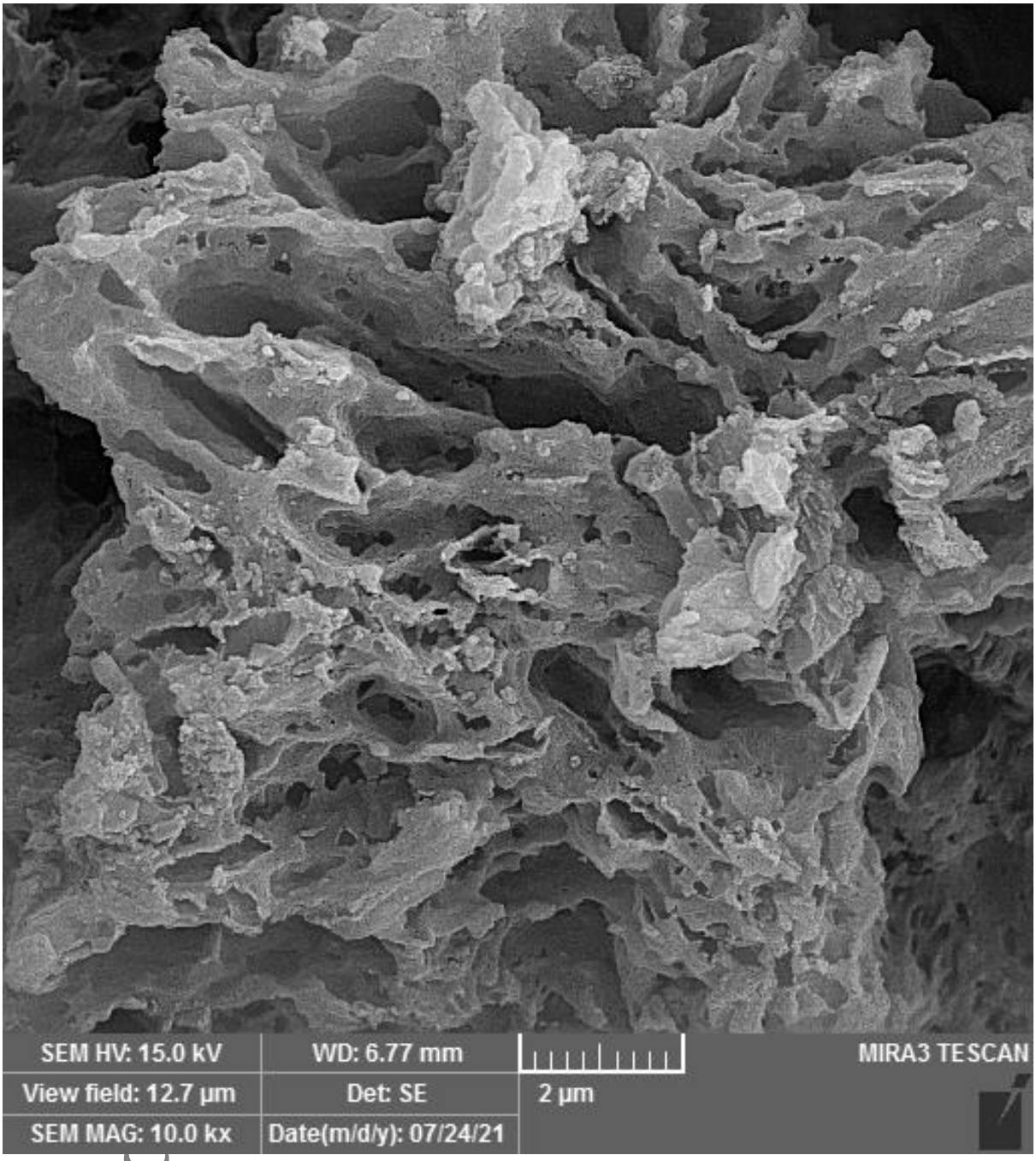
SEM HV: 15.0 kV
WD: 6.77 mm
MIRA3 TESCAN
View field: 12.7 µm
Det: SE
2 µm
SEM MAG: 10.0 kx
Date(m/d/y): 07/24/21

(e)

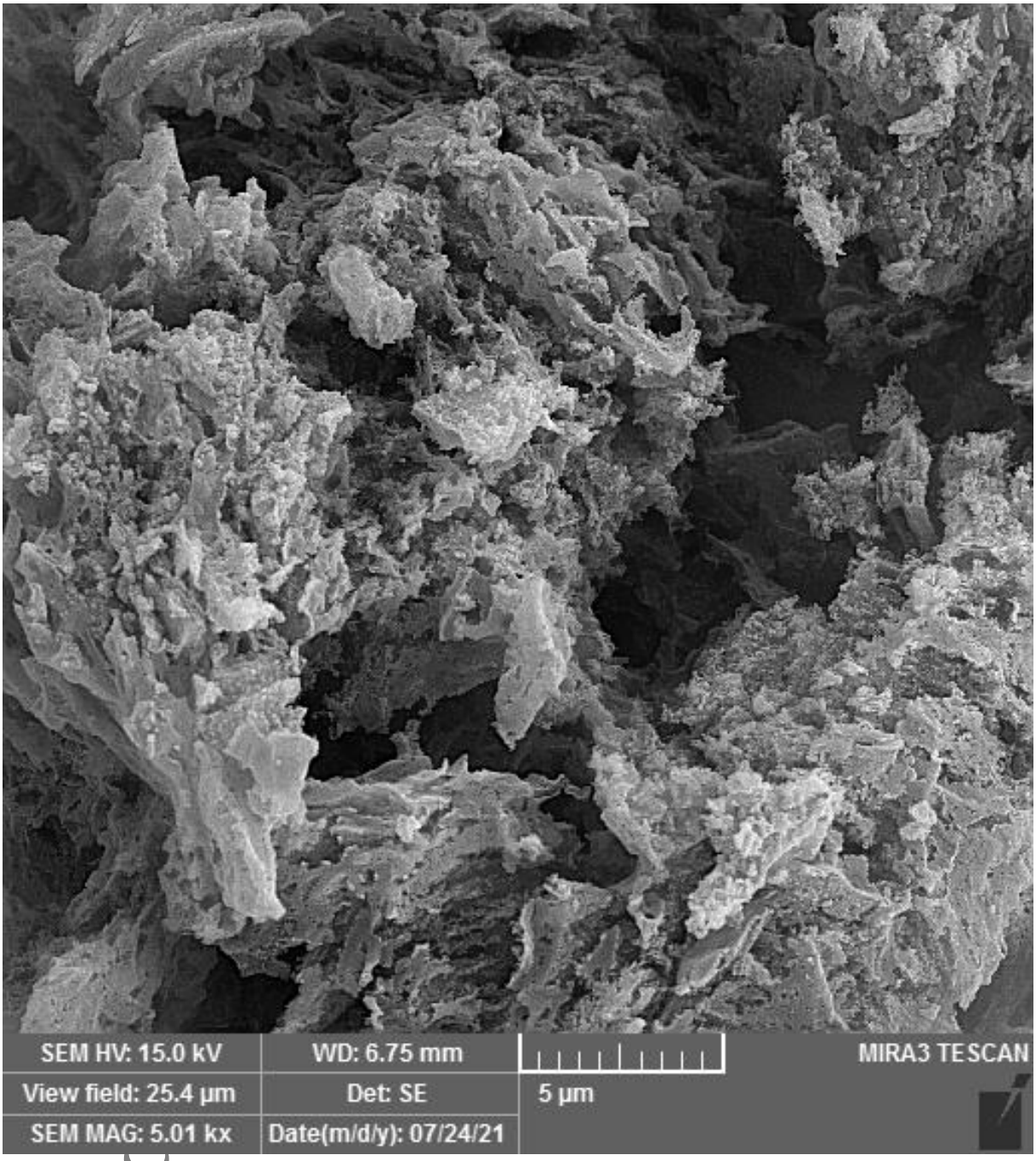

(f)

Fig. 4. SEM images of (a, b, and c) pure g-C_3N_4 and (d, e, and f) Fe(II)-g-C_3N_4

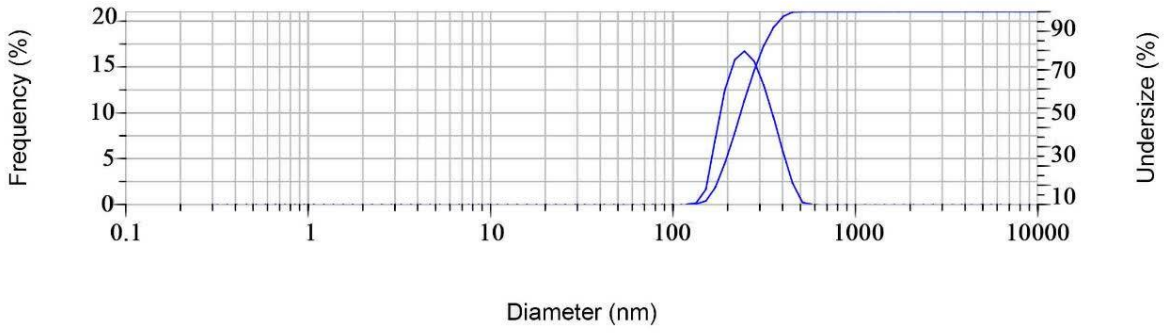

(a)

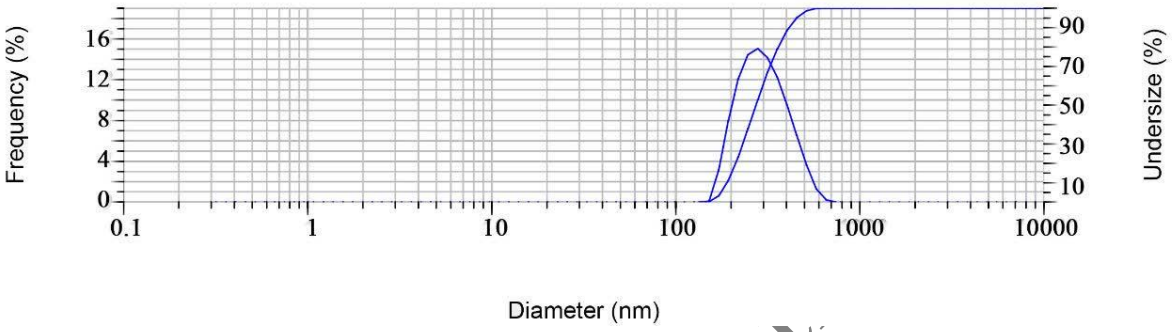

(b)

Fig. 5. Average particle size of (a) g-C_3N_4 and (b) Fe(II)-g-C_3N_4

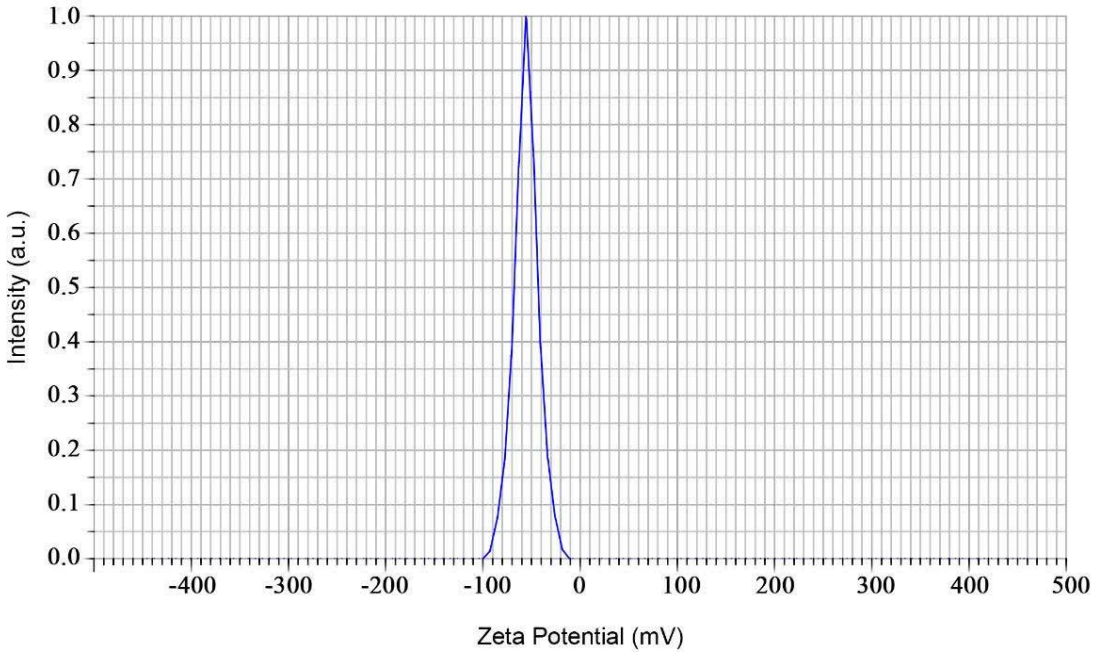

(a)

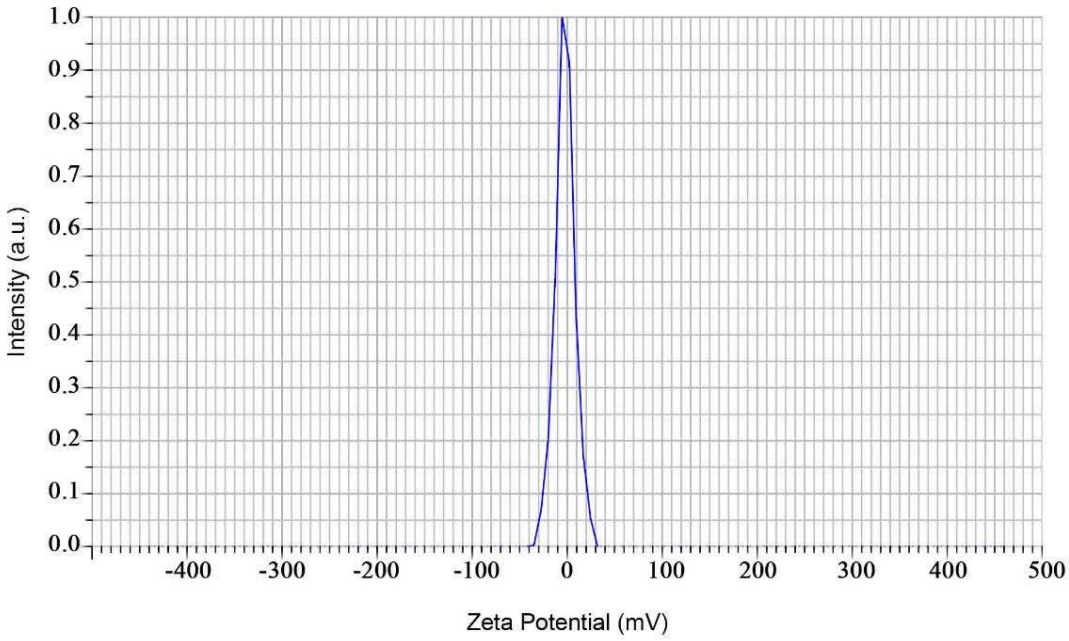

(b)

Fig. 6. Surface load of (a) g-C_3N_4 and (b) Fe(II)-g-C_3N_4

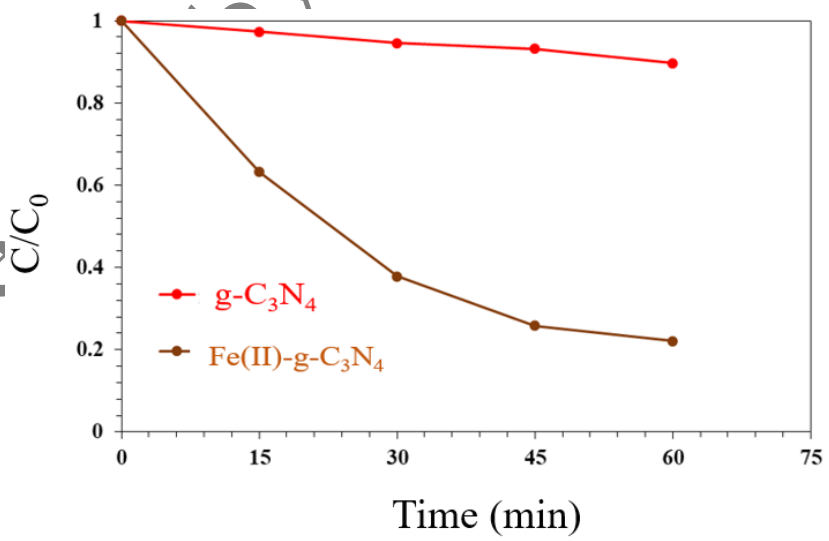

Fig. 7. Cr(VI) removal using Fe(II)-g-C_3N_4 and g-C_3N_4

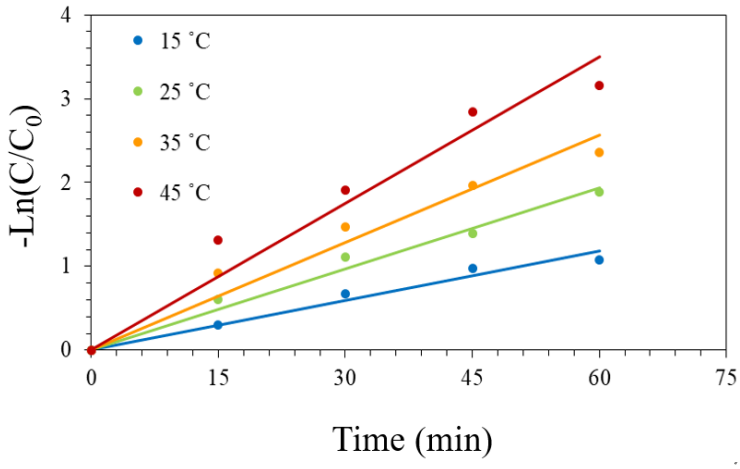

Fig. 8. Effects of temperature on the kinetics of Cr(VI) removal by Fe(II)-g-C_3N_4 (pH: 5; Cr(VI) concentration: 50 ppm in deionized water; Fe(II)-g-C_3N_4 concentration: 2 $g.L^{-1}$; mixing with a shaking incubator at 250 rpm).

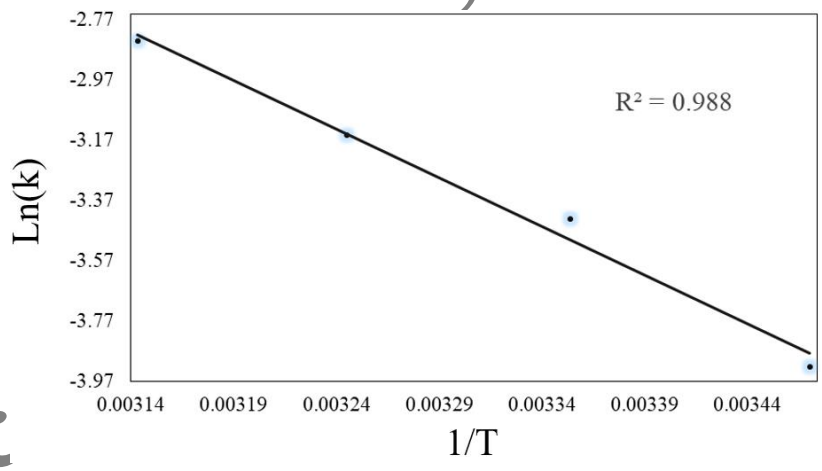

Fig. 9. Relationship between k_{obs} and temperature to obtain E_a

Table 1. The influence of pH values on the Cr(VI) removal using Fe(II)-g-C_3N_4

pH	k_{obs} (min^{-1})	$t_{1/2}$ (min)	r^2	Removal (%)
4	0.0327	21.19	0.9678	82.1
5	0.0258	26.86	0.9709	75.9
7	0.0112	69.31	0.9653	46.3
8	0.0062	111.79	0.9456	31.7

Table 2. The influence of Fe(II)-g-C_3N_4 concentration on the kinetics of Cr(VI) removal

Concentration of Fe(II)-g-C_3N_4 ($g.L^{-1}$)	k_{obs} (min^{-1})	$t_{1/2}$ (min)	r^2	Removal (%)

1	0.0154	45.01	0.9851	59.8
1.5	0.0253	27.39	0.9715	75.3
2	0.0393	17.54	0.9484	88.8
2.5	0.0481	14.41	0.953	93.2

Table 3. The impact of temperature on the kinetics of Cr(VI) removal

Temperature (°C)	**k_{obs} (min^{-1})**	**$t_{1/2}$ (min)**	**r^2**	**Removal (%)**
15	0.0198	35	0.9661	65.6
25	0.0324	21.4	0.9804	84.7
35	0.0427	16.2	0.9555	90.6
45	0.0584	11.86	0.9395	95.7

Table 4. The impact of Cr(VI) concentration on the kinetics of Cr(VI) removal

Cr(VI) concentration (ppm)	k_{obs} (min^{-1})	$t_{1/2}$ (min)	r^2	Removal (%)
30	0.0835	8.3	0.9671	99
50	0.0509	13.61	0.9483	93.9
70	0.0297	23.33	0.9612	80.7

Biography

Milad Fathi obtained his MS in Chemical Engineering from the University of Mohaghegh Ardabili, Ardabil, Iran in 2021. His activities focused on experimental studies of water treatment, focusing on the heavy metal removal from water, and the development of process simulation and modeling.

Aziz Babapoor, PhD, is a full-time Professor in the Chemical Engineering Department of the University of Mohaghegh Ardabili, Ardabil, Iran. The authorship of 35 books in Iranian and international publications and more than 100 ISI articles (focusing on wastewater treatment and energy storage) are among his research records. He is also the head of the mineral water and drinking department of the Water and Mineral Water Engineering Research Institute. Selection as the world's top 2% scientist in 2020-2024 is one of his honors.

Zohreh Rahimi-Ahar, PhD, is a full-time Assistant Professor in the Chemical Engineering Department of Velayat University, Iranshahr, Iran. She obtained her PhD degree in Chemical Engineering from the University of Isfahan in October 2018. Her activities focused on experimental studies of desalination systems, water treatment, and the development of process simulation and modeling. She has more than 30 papers on water treatment and desalination systems in high-ranking journals. By combining these investigations, she aims to gain a comprehensive understanding of the chances of water treatment mechanisms and environmental protection.

Hadi Basharnavaz, PhD, is a full-time Assistant Professor in the Chemistry Department of Yazd University, Iran. He obtained her PhD degree in Physical Chemistry from Kashan University in October 2016. He has more than 40 papers in international journals.